metals

MDPI

Article

Effect of Composition and Microstructure on Hydrogen Damage Behavior of Pipeline Steel

Weiwei Zhang [1,2], Linjun Zhou [3], Xiqian Song [3], Guoliang Zhang [3], Pengcheng Zhang [3] and Huibin Wu [3,*]

[1] School of Materials Science and Engineering, Xi'an University of Architecture and Technology, Xi'an 710055, China; zhangweiwei008@cnpc.com.cn
[2] State Key Laboratory of Service Behavior and Structure Safety for Petroleum Tubular Goods and Equipment Materials, CNPC Tubular Goods Research Institute, Xi'an 710077, China
[3] Collaborative Innovation Center of Steel Technology, University of Science and Technology Beijing, Beijing 100083, China
* Correspondence: wuhb@ustb.edu.cn

Abstract

Hydrogen energy represents a crucial clean energy carrier and plays a critical role in achieving the national strategic goals of carbon neutrality and peak carbon emissions. Pipeline transportation is currently the most economical and efficient method for hydrogen delivery. However, most existing hydrogen pipelines worldwide utilize low-alloy steels, which are prone to hydrogen embrittlement (HE) during hydrogen transportation, leading to degradation of mechanical properties in pipeline steels. Since material composition and microstructure directly govern pipeline steel performance, this study systematically investigates the effects of compositional variations among three X65-grade pipeline steels on their microstructural evolution and hydrogen embrittlement resistance. Key findings include reducing Mn content enhances hydrogen embrittlement resistance by refining grain size and increasing the proportion of low-angle grain boundaries (LAGBs); cementite phases act as preferential hydrogen trapping sites, significantly reducing hydrogen resistance; and strain rate dependency of HE susceptibility is confirmed, as under slower strain rates, hydrogen interacts with dislocations, promoting brittle fracture mechanisms. This work provides practical mechanism insights for optimizing hydrogen-resistant pipeline steel design through compositional regulation and microstructural engineering.

Keywords: hydrogen embrittlement; pipeline steel; slow strain rate tensile; microstructure

Check for updates

Academic Editor: Jin-Yoo Suh

Received: 29 April 2026
Revised: 31 May 2026
Accepted: 1 June 2026
Published: 8 June 2026

Copyright: © 2026 by the authors. Licensee MDPI, Basel, Switzerland. This article is an open access article distributed under the terms and conditions of the Creative Commons Attribution (CC BY) license.

1. Introduction

As a critical clean energy source, hydrogen energy plays a pivotal role in facilitating the green transition and meeting sustainable development goals [1–3]. Among existing transportation methods, pipeline delivery demonstrates significant economic and efficiency advantages for large-scale, long-distance hydrogen transport [4–6]. However, during hydrogen transportation via pipelines, the steel is continuously exposed to hydrogen environments. Hydrogen molecules adsorb onto the steel surface, dissociate into hydrogen atoms, permeate into the steel matrix, and subsequently diffuse, accumulate, and interact with metallic lattice structures [7–9]. The progressive degradation of mechanical properties in pipeline steel caused by this microcrack propagation process is termed hydrogen embrittlement (HE) [10–13]. Given the unpredictable structural damage caused by HE, comprehensive research on the impact of hydrogen on the performance of pipeline steel is imperative to enhance HE resistance and ensure safe and efficient applications.

As the core material for pipeline transportation, the HE susceptibility of pipeline steel is strongly influenced by composition and microstructure. Ghosh et al. [14] investigated the role of S in HE susceptibility, finding that sulfur readily combines with Mn to form MnS inclusions. These inclusions act as crack nucleation sites and exacerbate sensitivity to HE. Yan et al. [15] reported that Mn significantly affects the HE susceptibility of X65 steel; elevated Mn content promotes elongated Mn-Nb-S polygonal inclusions, which detach easily and induce microvoid formation and stress concentration, thereby increasing HE susceptibility. Extensive studies in metallic materials engineering have demonstrated that non-metallic inclusions exacerbate HE susceptibility by inducing localized stress concentration and lattice defects, while strategic inclusion modification effectively mitigates HE risks [16–22]. Research by Ran et al. [23] on Nb-V microalloying in X52 pipeline steel demonstrates that this alloy design effectively reduces hydrogen embrittlement susceptibility through three synergistic mechanisms: nano-scale secondary phase precipitation, monophasic microstructure formation, and refined grain structure. Zha et al. [24] studied the correlation between microstructure heterogeneity and HE susceptibility in X65 steel. Their work revealed that the outer layer, characterized by finer grains and higher densities of grain boundaries and dislocations, traps more hydrogen and impedes its diffusion. In contrast to the inner layer, where grain boundaries act as hydrogen diffusion pathways, grain boundaries in the outer layer serve as hydrogen traps, resulting in lower HE susceptibility in the outer layer compared to the inner layer. Lv et al. [25] explored hydrogen environment effects on crack initiation and propagation in X65 steel, concluding that microstructural features govern crack initiation (with inclusions as nucleation sources) and crack propagation tendencies (influenced by pearlite morphology). Jack et al. [26] similarly demonstrated that ferrite-pearlite microstructures promote substantial hydrogen uptake and trapping, accelerating HE. These studies collectively underscore the critical role of material composition and microstructure in HE susceptibility, yet mechanistic insights remain insufficiently explored.

Current HE research methodologies primarily combine electrochemical hydrogen charging with slow strain rate tensile (SSRT) testing, where steels are strained at a constant, low rate. However, systematic investigations on strain rate-dependent HE susceptibility are limited. Shishvan et al. [27] developed models to predict strain rate sensitivity in HE, while Peng et al. [28] examined strain rate effects on X80 steel's HE resistance in gaseous hydrogen, concluding that slower strain rates reduce ductility and elevate HE susceptibility. Nonetheless, the impact of strain rate on pipeline steel under electrochemical hydrogen charging remains poorly understood.

Therefore, this study evaluates HE susceptibility in experimental steels via electrochemical hydrogen charging-coupled SSRT. Advanced characterization techniques—including scanning electron microscopy (SEM), electron backscatter diffraction (EBSD), transmission electron microscopy (TEM), and electron probe microanalysis (EPMA) are employed to elucidate the influence of composition and microstructure on HE resistance. In particular, the hydrogen microprinting technique (HMT) is used to directly visualize the spatial distribution of hydrogen in the microstructure, which provides intuitive evidence for hydrogen trapping behavior [29,30]. Additionally, SSRT tests under varying strain rates are conducted to quantify strain rate-dependent HE susceptibility.

2. Materials and Methods

2.1. Material

The steels used in this experiment were pipeline steels obtained through thermomechanically controlled processing, with their primary chemical composition listed in Table 1.

The hot rolling process parameter range is listed in Table 2. The thickness of the steel plate is 18 mm. The experimental X65 pipeline steel is provided by domestic steel mills.

Table 1. Chemical composition of the X65 pipe steel (wt.%).

Steel	C	Mn	P	S	Si	Ni	Cr	Cu	Al	Nb	Mo	V	Ti
1	0.0495	1.272	0.0065	0.0015	0.189	0.15	0.238	0.02	-	0.04	0.0094	0.0337	0.0119
2	0.055	1.63	0.009	0.0012	0.25	0.01	0.26	0.02	0.028	0.043	0.003	0.004	0.013
3	0.040	0.80	0.008	0.0006	0.26	0.21	0.33	0.02	0.032	0.048	0.180	0.055	0.012

Table 2. Hot rolling process parameters.

Process	Parameter Ranges	Allowable Deviation
Reheating Temperature	1180~1200 °C	±10 °C
Slab Soaking Time	10~15 min/cm	0~60 min
Rolling Technology	Two-stage controlled rolling process	
Total roughing Rolling Reduction ratio	70~80%	±1%
Roughing Delivery Thickness	(3.0~3.2) h	(0~0.2) h
Total Finishing Rolling Reduction Ratio	65~75%	±1%
Finishing Rolling Entry Temperature	880~910 °C	±10 °C
Finishing Rolling Temperature	820~860 °C	±20 °C
Final Cooling Temperature	500~540 °C	±20 °C
Cooling Rate	15~25 °C/s	±3 °C/s
Total Number of Rolling Passes	12	0

2.2. SSRT Testing

SSRT testing was conducted using electrochemical hydrogen charging coupled with SSRT testing. Figure 1 illustrates the geometry and dimensions of the SSRT testing steel; the steel thickness is 2 mm. The steel dimensions are illustrated in Figure 1. The electrochemical solution comprised 0.2 mol/L H_2SO_4 + 0.22 g/L thiourea, with a current density of 5 mA/cm^2 and strain rates of 2×10^{-5} s^{-1} and 5×10^{-5} s^{-1}. Post-machining, all steels were meticulously ground along their axial direction using fine sandpaper up to 2000#. All SSRT trials under each group condition were repeated at least three times to ensure reproducibility, and the standard deviation of all data was less than 1%, indicating good reproducibility.

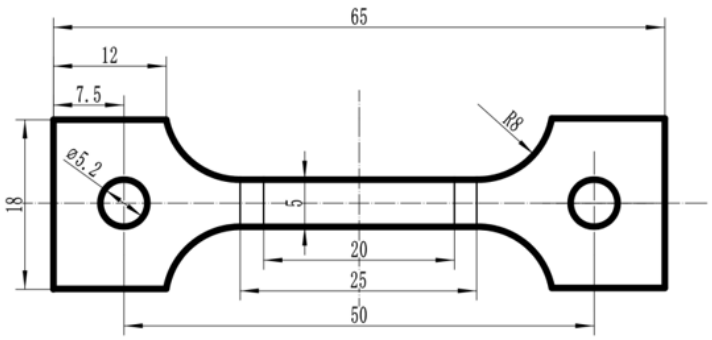


Figure 1. Dimensions of the SSRT test steel (unit: mm).

2.3. Microstructural Analyses

Microstructural characterization and tensile fracture morphology analysis were performed using a ZEISS GeminiSEM 500 SEM (Carl Zeiss, Oberkochen, Germany) operating at 15 kV accelerating voltage and 60 μm aperture size.

Steel was electrolytically polished with a 10% perchloric acid-alcohol solution under conditions of 22 V voltage, 1 A current, and 35 s duration. EBSD analysis was conducted to examine crystallographic structures, employing a 20 kV accelerating voltage and 120 μm aperture size.

Initial steels (10 mm × 10 mm × 0.3 mm) were prepared via wire cutting, mechanically thinned to 50 μm thickness, and punched into 3 mm-diameter disks. Double-jet electropolishing was executed using a 5% perchloric acid-absolute ethanol electrolyte. Precipitate morphology and dislocation configurations were subsequently characterized using a TECNAI F20 TEM (FEI Company, Hillsboro, OR, USA).

EPMA element mapping was applied to metallographic steels to quantify segregation types and spatial distribution patterns of alloying elements.

2.4. Hydrogen Microprinting Test

To characterize the spatial distribution of hydrogen in the microstructure, Hydrogen Microprinting Tests were conducted. The specific experimental procedure was as follows:

First, metallographic samples of three types of steel plates were prepared, followed by 2 h of electrochemical hydrogen charging. The hydrogen charging solution was a 3.5 wt.% NaCl solution, and the hydrogen charging current density was set to 100 mA/cm^2. Subsequently, the samples were cleaned and dried thoroughly to remove the residual solution and impurities on the surface. Next, the samples were statically immersed in a reaction solution for 5 min. The chemical composition of the reaction solution was 0.5 g AgBr + 40 mL $NaNO_2$. During the reaction, Ag^+ ions in the solution were reduced to metallic silver by the hydrogen exuded from the sample surface and deposited on the sample surface. Thus, the distribution of silver particles indirectly reflects the distribution of hydrogen traps on the sample surface. Finally, the samples were rinsed in a cleaning solution and then dried. The chemical composition of the cleaning solution was 15 wt.%NaS_2O_3 + 10 wt.% $NaNO_2$.

3. Results

3.1. Microstructure Characterization

The SEM morphologies of the three steels are shown in Figure 2. All steels exhibit a similar ferrite + bainite microstructure, with uniform and refined microstructures, indicating that the increase in Mn content and Mo microalloying exerts a limited influence on the microstructural evolution.

To further characterize the microstructural features of the three steels, EBSD analysis was conducted. To rule out the presence of martensite-austenite (M-A) constituents, EBSD characterization was performed, as SEM observation is limited to naked-eye viewing. Figure 3 shows the comparative phase maps of the three steels. The results demonstrate that only BCC (Body-Centered Cubic) phase exists in all three steels, suggesting the absence of M-A constituents, consistent with SEM morphological observations. The formation of M-A constituents originates from carbon atom diffusion along γ-Fe/α-Fe phase boundaries during phase transformation, with subsequent enrichment in untransformed residual γ-Fe regions. Coarse and densely distributed M-A constituents typically act as hydrogen aggregation sites, promoting crack initiation and propagation, thereby enhancing material susceptibility to HE. These findings imply that the three steels exhibit improved resistance to HE.

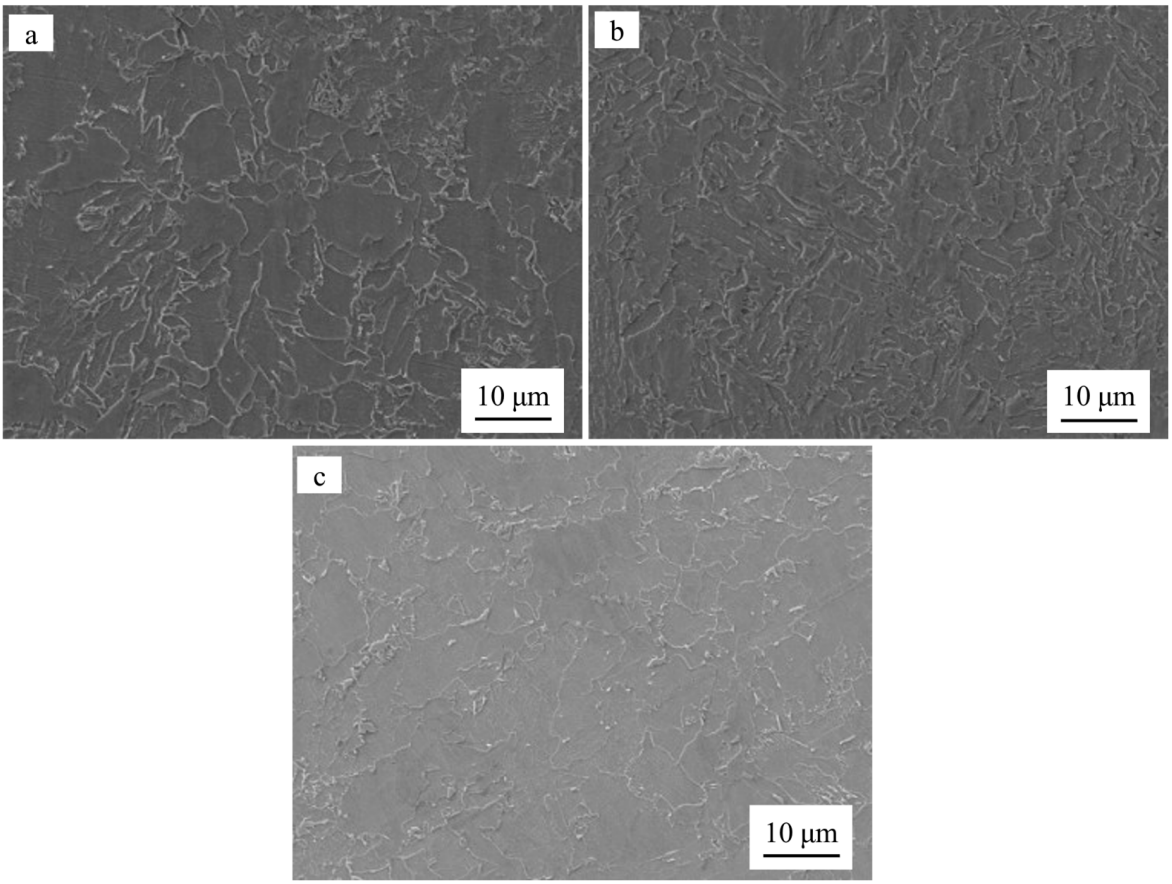


Figure 2. SEM morphologies of the three steels: (**a**) steel 1, (**b**) steel 2, (**c**) steel 3.

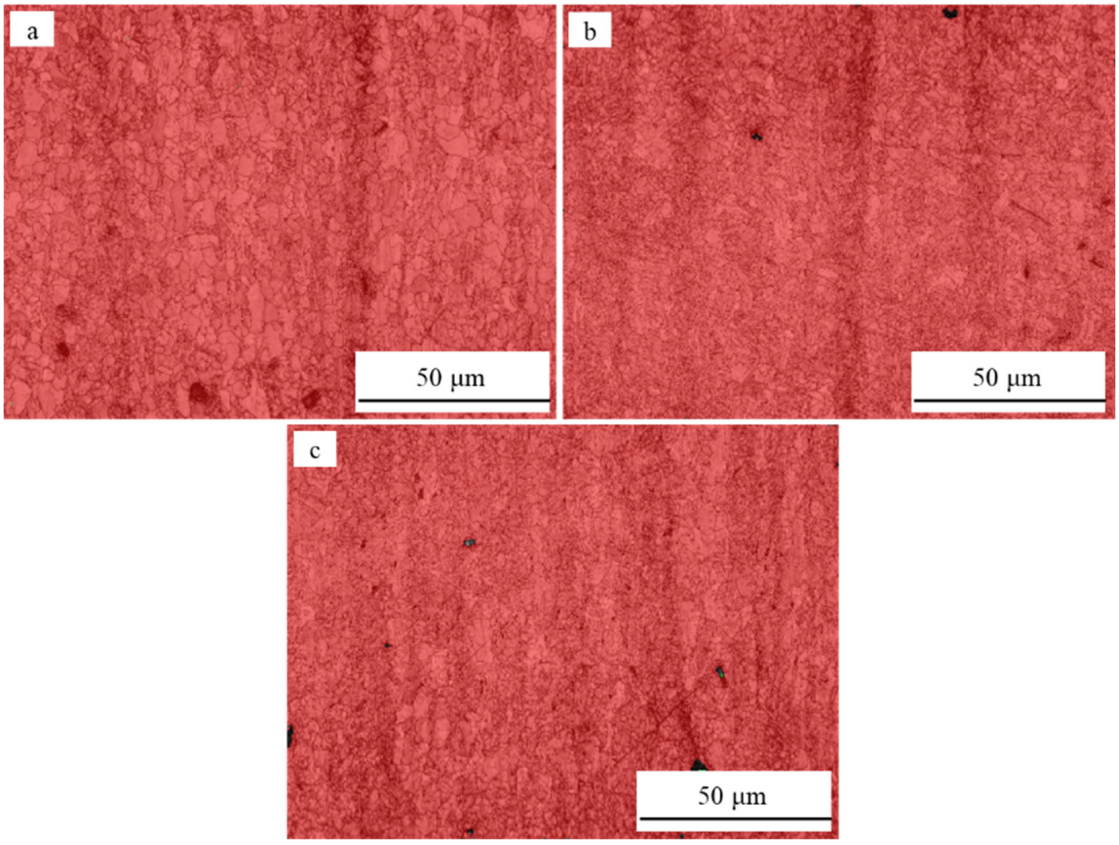


Figure 3. EBSD phase maps: (**a**) steel 1; (**b**) steel 2; (**c**) steel 3.

Figure 4 shows EBSD analysis results of the three steels. The results indicate that all three steels predominantly exhibit random crystallographic orientations. The average effective grain size is similar (steel 1—3.2 μm, steel 2—3.0 μm, steel 3—3.3 μm). Grain boundary misorientation analysis reveals the following distributions: steel 1: 47.2% high-angle grain boundaries (HAGBs) and 52.8% low-angle grain boundaries (LAGBs); steel 2: 33.3% HAGBs and 66.7% LAGBs; steel 3: 26.0% HAGBs and 74.0% LAGBs. Grain refinement and LAGBs critically influence hydrogen diffusion behavior. Chen et al. [31] proposed that LAGBs act as the dominant hydrogen trapping sites. Finer grains and higher LAGB density can trap more diffusible hydrogen atoms, thereby reducing localized hydrogen enrichment and concomitantly enhancing HE resistance.

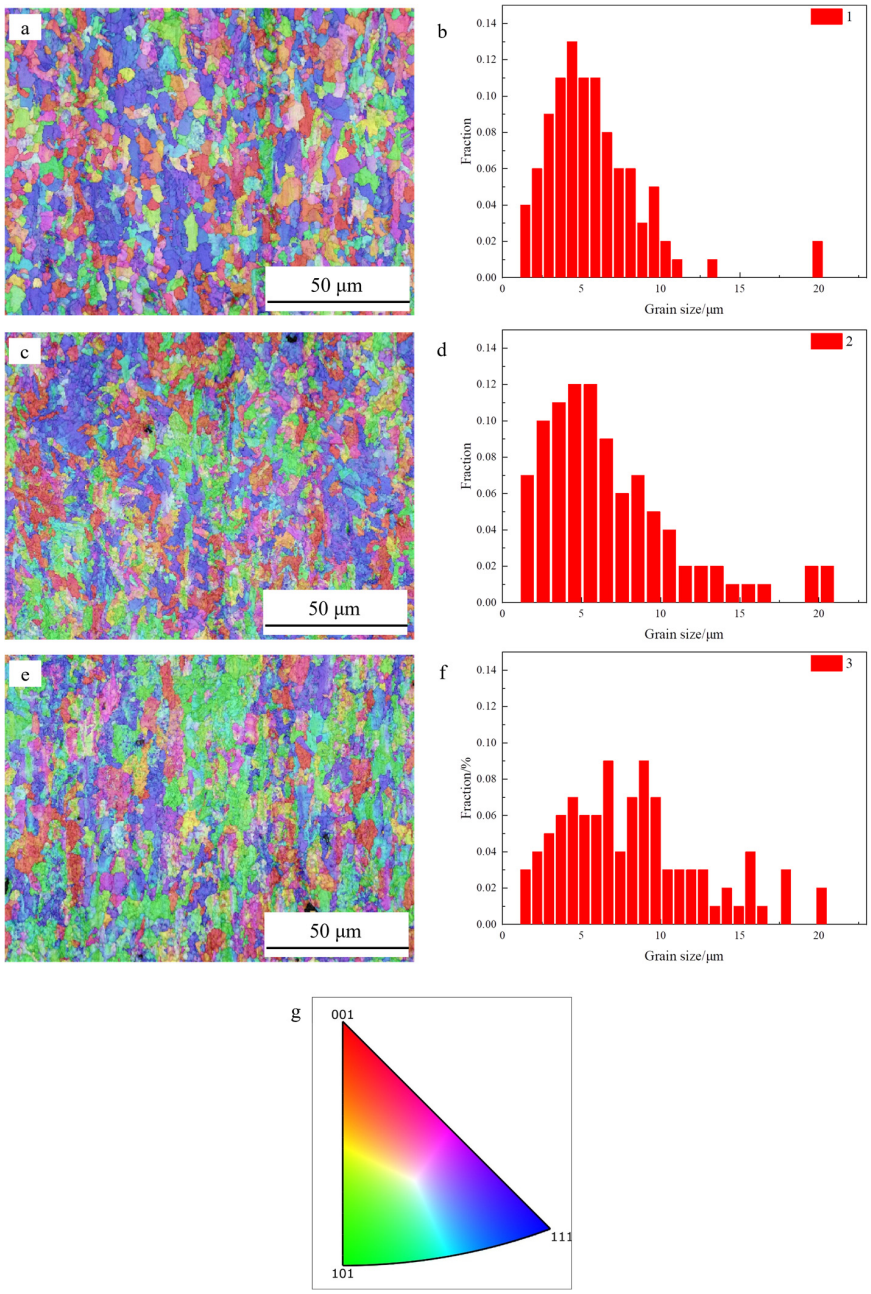


Figure 4. EBSD statistical maps: (**a**) IPF map of steel 1; (**b**) effective grain size distribution map of steel 1; (**c**) IPF map of steel 2; (**d**) effective grain size distribution map of steel 2; (**e**) IPF map of steel 3; (**f**) effective grain size distribution map of steel 3; (**g**) IPF key for all steels.

Figure 5 shows Kernel Average Misorientation (KAM) maps of the three steels. The KAM maps visualize lattice distortion gradients and reflect strain distribution within the microstructure, where the color gradient from blue to green, yellow, and finally red corresponds to an increasing KAM value. Nabizada et al. [32] found that the KAM values of the uncharged samples were lower than those of hydrogen-charged samples. Higher KAM values indicate greater localized strain. Analysis reveals that steel 1 exhibits inhomogeneous strain distribution compared to steels 2 and 3. A homogeneous distribution of hydrogen traps effectively disperses and captures hydrogen atoms, thereby preventing localized hydrogen aggregation at specific sites. This mechanism significantly enhances resistance to HE.

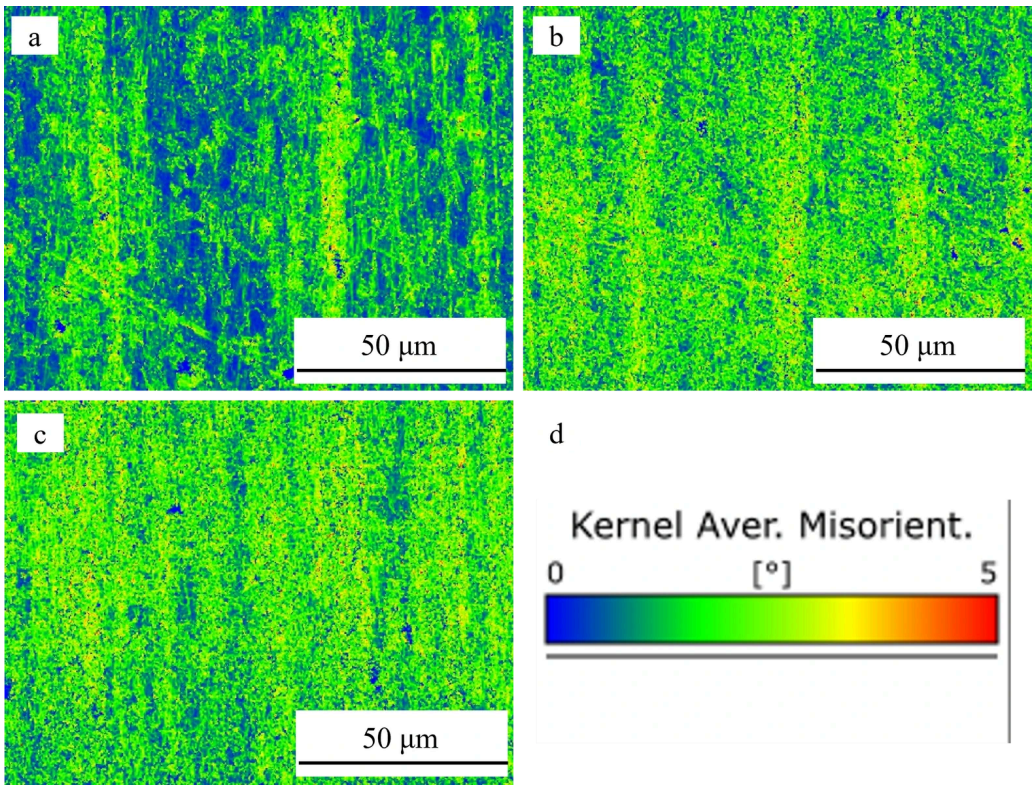


Figure 5. EBSD KAM maps: (**a**) steel 1; (**b**) steel 2; (**c**) steel 3; (**d**) legend.

Dislocation density critically influences HE susceptibility. To elucidate the mechanistic role of dislocations, TEM observations were conducted, as shown in Figure 6. The TEM micrographs of all three steels reveal high-density dislocation structures, characterized by densely distributed dislocation lines and tangles. As effective hydrogen traps, dislocations interact preferentially with hydrogen atoms. This interaction promotes uniform hydrogen trapping throughout the steel matrix, mitigating localized hydrogen accumulation. The TEM micrographs of steel 2 exhibit aligned lamellar cementite (Fe_3C) structures (Figure 7). Liu et al. [33] demonstrated that hydrogen can be captured by intragranular cementite precipitates. Due to the high binding energy of cementite hydrogen traps, adsorbed hydrogen is not prone to desorption. Such cementite phases are known to act as hydrogen accumulation sites, which can nucleate microcracks and accelerate their propagation, significantly degrading HE resistance.

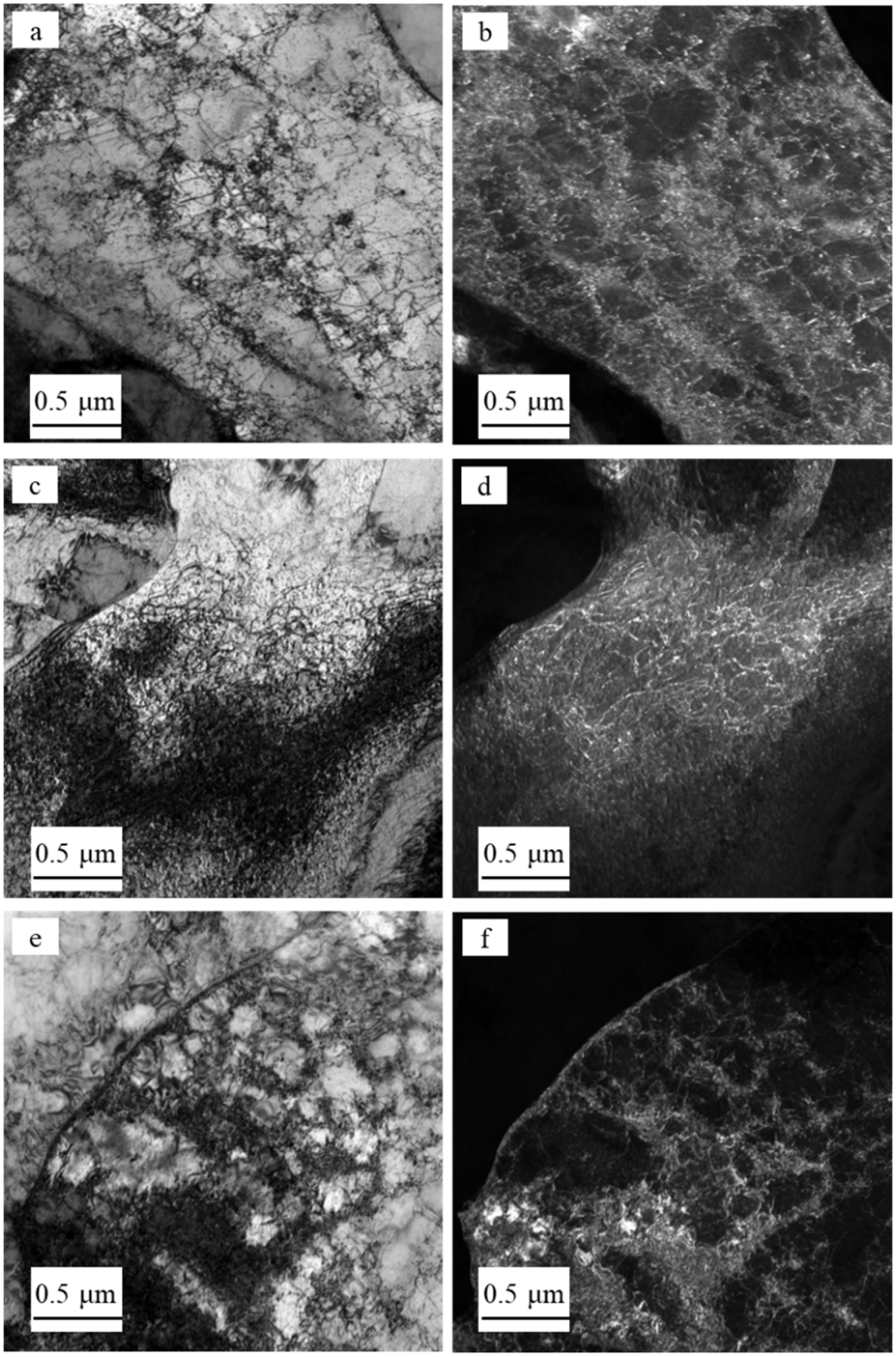


Figure 6. TEM micrographs of the three steels: (**a**) bright-field (BF) image of steel 1; (**b**) dark-field (DF) image of steel 1; (**c**) BF image of steel 2; (**d**) DF image of steel 2; (**e**) BF image of steel 3; (**f**) DF image of steel 3.

To investigate the elemental distribution in the three steels, EPMA was conducted, as shown in Figure 8. Analysis of C, Mn, and Mo elements revealed homogeneous elemental distribution across all steels, with no evidence of elemental segregation or enrichment.

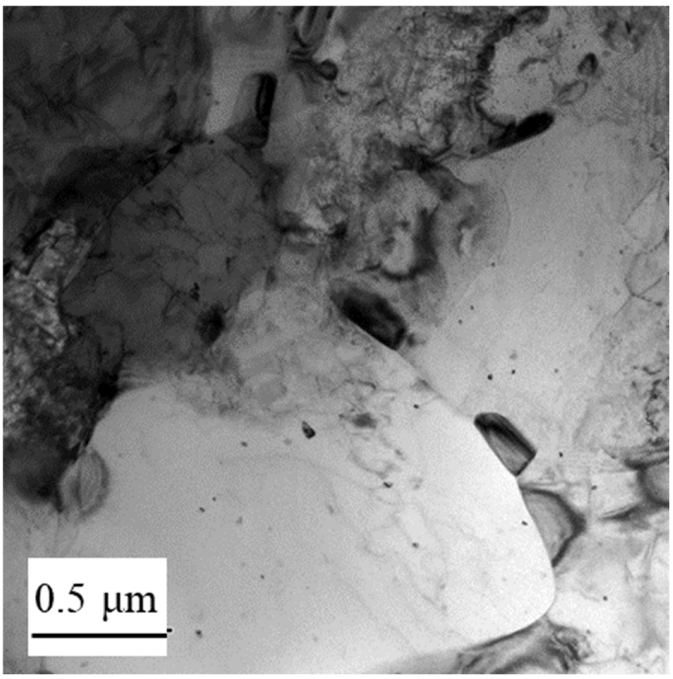


Figure 7. Cementite morphology in steel 2.

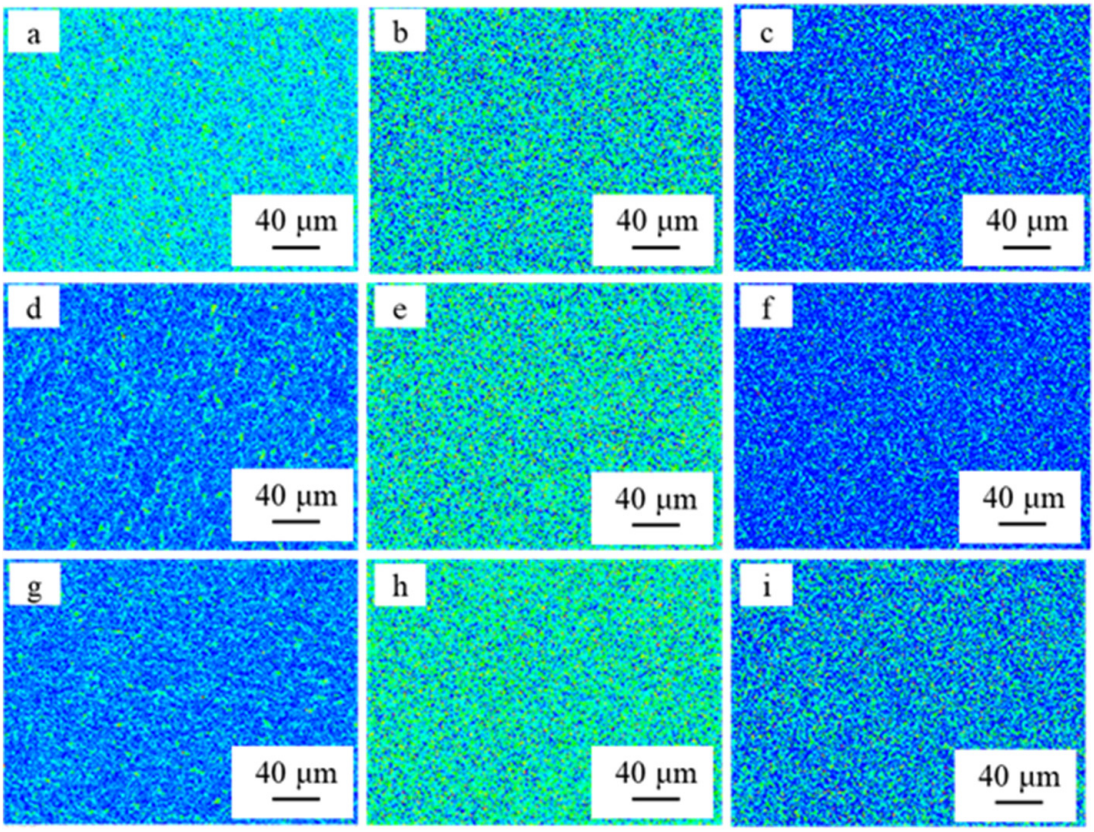


Figure 8. EPMA elemental mapping: (**a**) C distribution in steel 1, (**b**) Mn distribution in steel 1, (**c**) Mo distribution in steel 1, (**d**) C distribution in steel 2, (**e**) Mn distribution in steel 2, (**f**) Mo distribution in steel 2, (**g**) C distribution in steel 3, (**h**) Mn distribution in steel 3, and (**i**) Mo distribution in steel 3.

3.2. Hydrogen Distribution Inspection

Figure 9 shows the hydrogen microprint images and energy spectrum diagrams of three types of steel, respectively. From the energy spectrum, it can be determined that these white spots are particles of Ag.

It can be seen that the distribution positions of silver particles in the three types of steel plates are similar, mainly distributed in the finely divided structures, such as around bainite or inclusions, while there are few silver particles in ferrite. From the perspective of hydrogen embrittlement, the hydrogen enrichment in bainite grains, especially at the interface between bainite and ferrite, is the key factor affecting the hydrogen resistance of X65 steel. In comparison, hydrogen is enriched in hydrogen trap positions such as grain boundaries and bainite in all three types of steel.

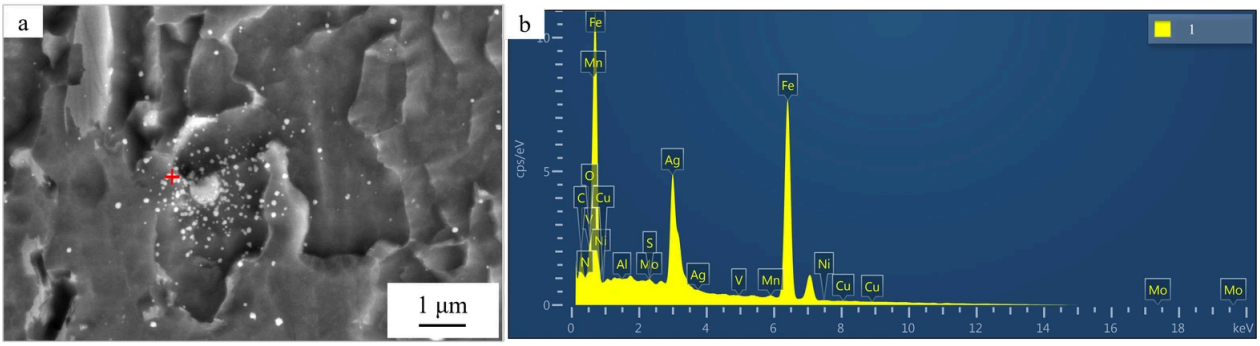


Figure 9. (**a**) Hydrogen microprint image of steel 1, (**b**) energy spectrum at the red-marked position.

3.3. SSRT Tests and Fracture Surface Analyses

SSRT tests and fracture surface analyses were conducted on three steels under three conditions: non-hydrogen-charged (strain rate 5×10^{-5} s^{-1}), hydrogen-charged at 5×10^{-5} s^{-1}, and hydrogen-charged at 2×10^{-5} s^{-1}. The post-fracture elongation results revealed that steel 1 exhibited 18.0 ± 0.5% elongation without hydrogen charging, 15.5 ± 0.6% at 5×10^{-5} s^{-1}, and 11.7 ± 0.8% at 2×10^{-5} s^{-1}, steel 2 showed 22.5 ± 0.4% (non-charged), 17.6 ± 0.7% (5×10^{-5} s^{-1}), and 16.3 ± 0.6% (2×10^{-5} s^{-1}), steel 3 recorded 17.1 ± 0.3% (non-charged), 16.9 ± 0.2% (5×10^{-5} s^{-1}), and 15.3 ± 0.5% (2×10^{-5} s^{-1}). These results demonstrate that HE significantly degrades material ductility, with greater ductility loss at 2×10^{-5} s^{-1} compared to 5×10^{-5} s^{-1}, indicating strain rate reduction exacerbates HE susceptibility. Comparative analysis of elongation reduction ratios (Figure 10) showed steel 3 exhibited the smallest overall ductility loss, while steel 1 displayed the maximum reduction (34.6%) at 2×10^{-5} s^{-1}, and steel 2 had the highest loss (21.7%) at 5×10^{-5} s^{-1}. Error bars represent standard deviation, not shown for brevity. The calculation formula is as follows:

$$I_\delta = \frac{L_0 - L}{L_0} \times 100\% \quad (1)$$

The SSRT results exhibit good repeatability in repeated tests under identical conditions. Due to different testing environments, obvious scatter is observed in the stress–strain curves between hydrogen-charged and control groups. Therefore, this paper uses elongation data with better repeatability to evaluate hydrogen embrittlement sensitivity.

Fractographic analysis of HE mechanisms was performed through observation of tensile fracture surfaces, as shown in Figures 11–13. Figure 11 presents SSRT fracture morphologies, where Figure 11b,d,f are magnified views of the central regions of steels 1, 2, and 3, respectively. All steels exhibited ductile fracture characteristics with well-defined dimples, indicating good intrinsic ductility. Figure 12 displays SSRT fracture surfaces at

a strain rate of 2×10^{-5} s^{-1}. Figure 12b,c show enlarged views of the edge and central regions of Figure 12a (steel 1). Hydrogen-charged steel 1 retained predominantly ductile fracture features with fine dimples, but distinct cleavage steps (brittle fracture morphology) were observed in the central region compared to the non-charged condition. Figure 12e,f correspond to the edge and central regions of Figure 12d (steel 2), revealing persistent ductile fracture characteristics with micro-dimples and no detectable brittle fracture signatures. Figure 12h,i magnify the edge and central regions of Figure 12g (steel 3). Hydrogen-charged steel 3 exhibited similar brittle fracture patterns in the central region as steel 1, demonstrating higher HE susceptibility in both steels due to insufficient resistance to hydrogen diffusion during electrochemical charging, ultimately leading to brittle failure.

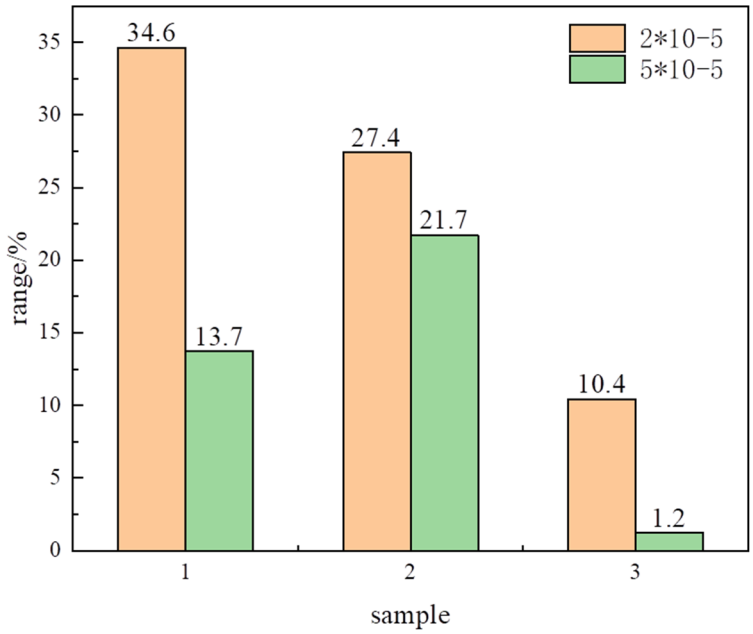


Figure 10. Post-fracture elongation reduction.

However, observations of the fracture morphologies at a strain rate of 5×10^{-5} s^{-1}, as shown in Figure 13, reveal that all three hydrogen-charged steels still exhibit ductile fracture characteristics in their central regions (Figure 13b,d,f), with clearly visible fine dimples. Notably, no cleavage steps are observed compared to the 2×10^{-5} s^{-1} strain rate condition.

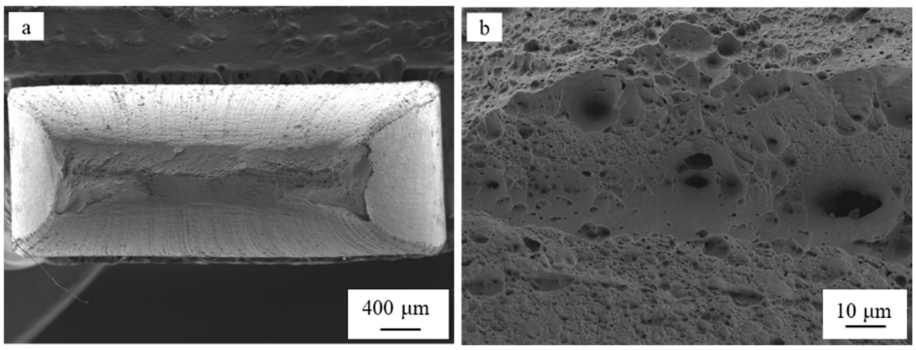


Figure 11. *Cont.*

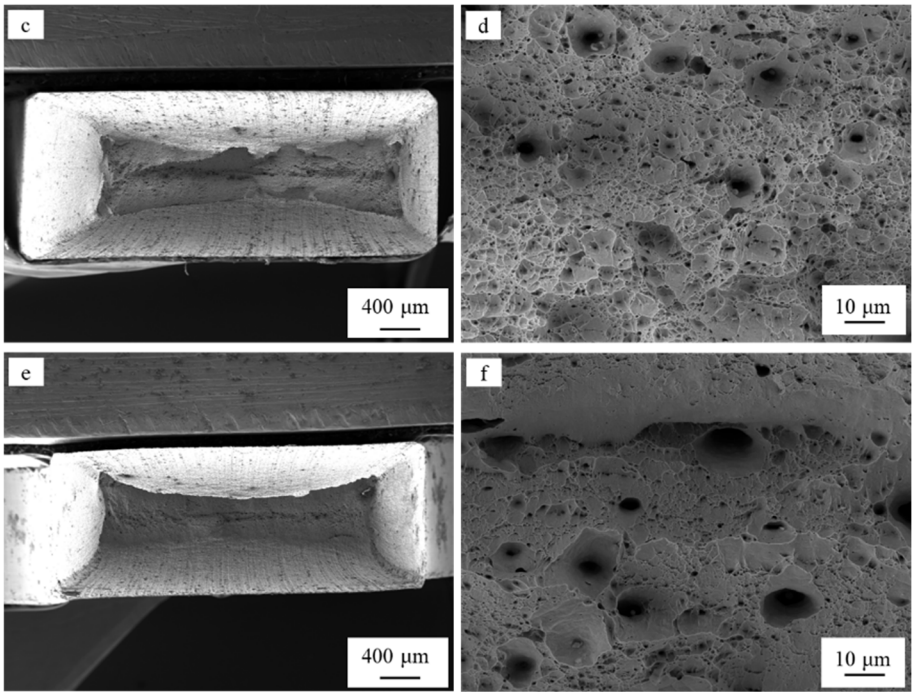


Figure 11. Fracture morphologies of non-hydrogen-charged steels under SSRT conditions: (**a**) Macro-morphology of steel 1, (**b**) magnified view of steel 1, (**c**) macro-morphology of steel 2, (**d**) magnified view of steel 2, (**e**) macro-morphology of steel 3, and (**f**) magnified view of steel 3.

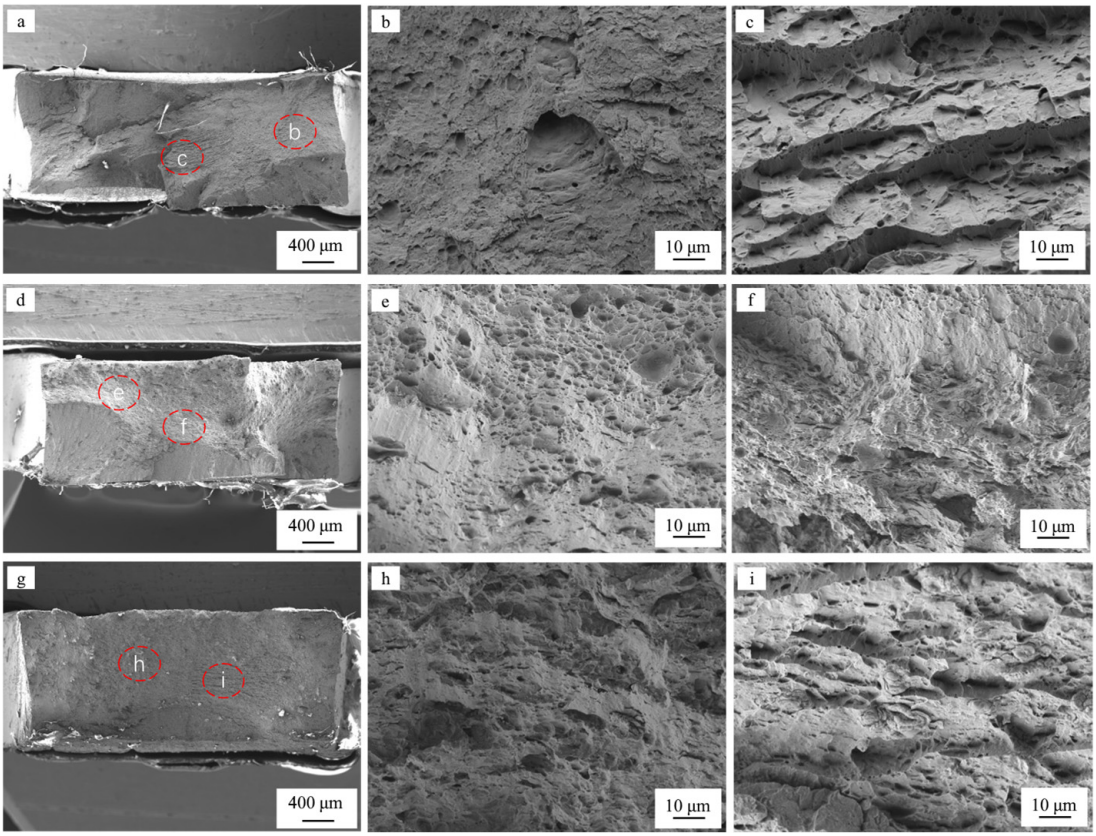


Figure 12. Fracture morphologies under slow strain rate tensile testing at 2×10^{-5} s^{-1}: (**a**) Macro-morphology of steel 1, (**b**) magnified view of the edge region of steel 1, (**c**) magnified view of the central region of steel 1, (**d**) Macro-morphology of steel 2, (**e**) magnified view of the edge region of steel 2, (**f**) magnified view of the central region of steel 2, (**g**) Macro-morphology of steel 3, (**h**) magnified view of the edge region of steel 3, and (**i**) magnified view of the central region of steel 3.

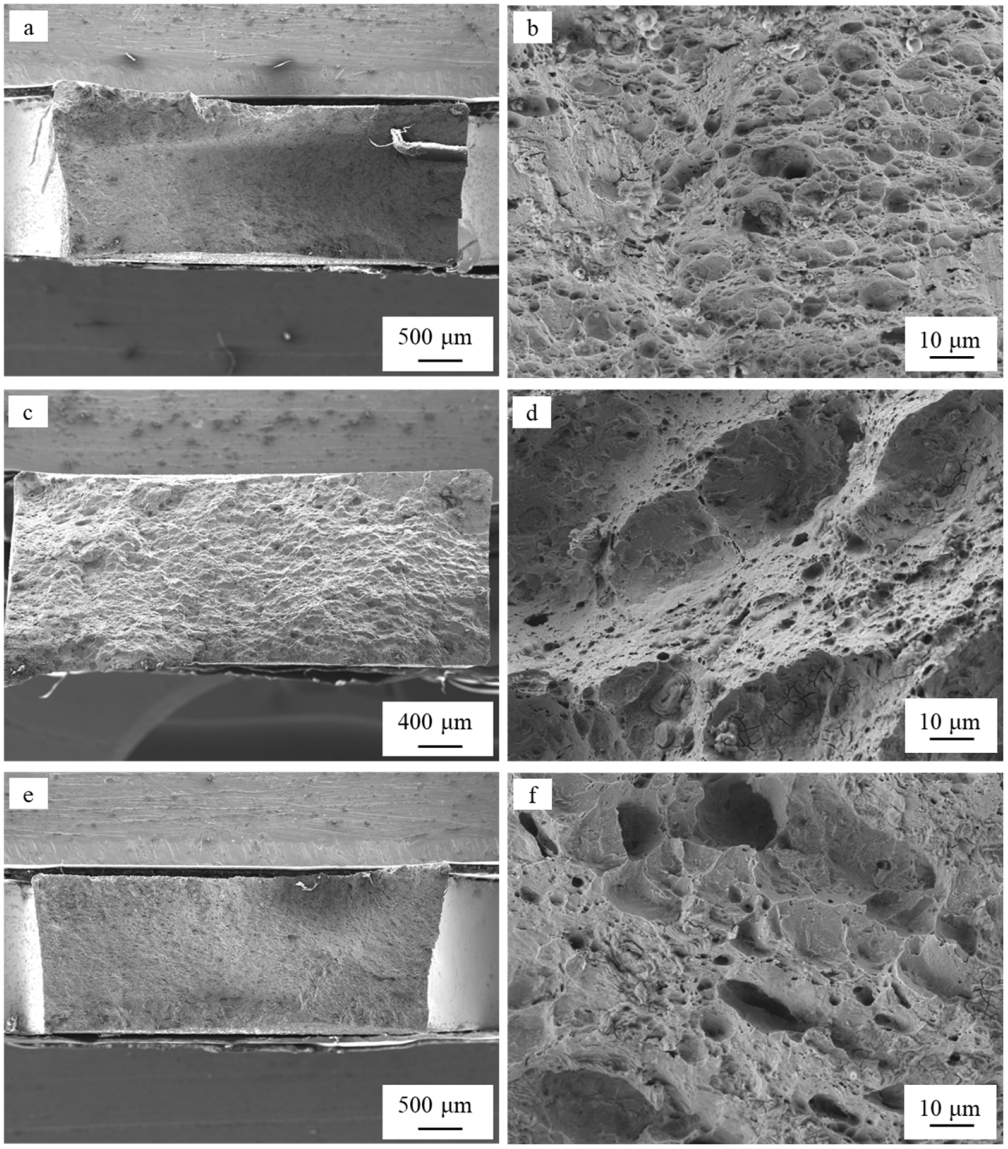


Figure 13. Fracture morphologies under slow strain rate tensile testing at 5×10^{-5} s^{-1}: (**a**) Macro-morphology of steel 1, (**b**) magnified view of steel 1, (**c**) Macro-morphology of steel 2, (**d**) magnified view of steel 2, (**e**) Macro-morphology of steel 3, (**f**) magnified view of steel 3.

4. Discussion

4.1. Influence of Composition and Microstructure on HE Susceptibility

Combining microstructural observations, EBSD analysis, TEM characterization, EPMA results, Hydrogen Microprinting Test and SSRT test data, steel 3 exhibits the lowest HE susceptibility. The core mechanism underlying this behavior is rooted in the synergistic interplay of microstructure, hysdrogen enrichment behavior, and hydrogen embrittlement fracture mechanisms mediated by compositional regulation.

Hydrogen microprint characterization directly visualized the hydrogen enrichment behavior of the three test steels. Hydrogen was mainly enriched around bainite and at inclusion-matrix interfaces, with scarce Ag particles observed in the ferrite matrix. This demonstrates that bainite/ferrite boundaries and grain boundaries are the dominant hydrogen trapping sites in X65 steel, and localized hydrogen accumulation at these sites is the key prerequisite for hydrogen embrittlement failure. The overall density of hydrogen-enriched zones in Steel 3 was markedly lower than that in Steels 1 and 2, providing intuitive visual evidence for its minimal hydrogen embrittlement susceptibility.

Mn refines grain size, and steel 2 with higher Mn content shows the smallest grain size. Campari et al. [34] reported that grain refinement significantly affects HE: finer grains introduce more grain boundaries to hinder hydrogen diffusion but also create additional hydrogen trapping sites. Among the three steels, Steel 3 contains the highest Mo content (0.180 wt.%) and exhibits the best hydrogen embrittlement resistance. The beneficial role of Mo in reducing HE susceptibility has been increasingly recognized. Mo contributes through multiple mechanisms: (i) Mo atoms segregate at grain boundaries, enhancing boundary cohesion and hindering hydrogen-induced decohesion [35], (ii) Mo participates in forming (Nb,Mo)C or MoC nano-precipitates, which act as effective hydrogen traps and reduce hydrogen diffusivity [36], and (iii) solute Mo atoms in the ferrite matrix serve as distributed trapping sites, retarding localized hydrogen enrichment [37]. In addition, the relatively low Mn content (0.80 wt.%) in Steel 3 further reduces the risk of MnS inclusions that act as crack nucleation sites. Therefore, the combination of Mo microalloying and low Mn design contributes synergistically to the superior HE resistance of Steel 3.

Zhang et al. [38] demonstrated that in X65 pipeline steel weldments, martensite/austenite constituents serve as preferential sites for hydrogen-induced cracking, with the weld metal exhibiting the highest HE susceptibility due to the presence of M/A constituents. TEM analysis revealed aligned cementite particles in steel 2, which act as hydrogen aggregation sites, promoting microcrack initiation/propagation and degrading HE resistance, consistent with its significant post-hydrogen-charging elongation reduction. The hydrogen microprint results also verified the remarkable characteristics of hydrogen enrichment at the second phase interfaces. However, the refined grains in steel 2 delayed hydrogen diffusion, explaining the absence of cleavage steps (brittle fracture) at slow strain rates. Steel 1 exhibited a higher proportion of HAGBs and heterogeneous strain distribution via EBSD. HAGBs, with higher interfacial energy, serve as preferential hydrogen adsorption sites, while strain localization exacerbates hydrogen aggregation, weakening grain boundary cohesion and initiating cracks, aligning with SSRT results. In contrast, steel 3 contained the highest fraction of LAGBs and dislocation cells observed by TEM, both effective in trapping hydrogen and impeding its diffusion, thereby enhancing HE resistance. Zhang et al. [39] revealed that reversible hydrogen traps are primarily associated with LAGBs and dislocations, whereas irreversible traps are predominantly attributed to HAGBs and precipitates. The higher proportion of LAGBs in the outer layer of X65 pipeline steel exhibited lower hydrogen diffusivity and enhanced hydrogen trapping capability, leading to reduced HE susceptibility compared to the inner layer.

4.2. Strain Rate Effects on HE Susceptibility

Despite superior HE resistance, steel 3 displayed cleavage steps at lower strain rates, a strain-rate-dependent phenomenon. Under slow strain rates, hydrogen-dislocation interactions at interfaces alter fracture mechanisms [40]. Hydrogen impedes dislocation motion, promoting its own diffusion. During in situ electrochemical SSRT, such interactions enable hydrogen penetration into the material interior, forming internal cracks that manifest as cleavage steps in the central regions of steels 1 and 3.

5. Conclusions

In situ electrochemical SSRT testing combined with fracture morphology analysis and multi-scale characterization reveals the hydrogen damage behavior of pipeline steels. The key conclusions are as follows:

1. The steel with low Mn and micro-Mo alloying demonstrates superior HE resistance, attributed to its high fraction of LAGBs, refined grain size, and dislocation

cell structures, which collectively enhance hydrogen trapping efficacy and inhibit hydrogen diffusion.

2. Compositional effects on HE resistance primarily manifest through grain refinement and LAGB density modulation. Grain refinement introduces both hydrogen diffusion barriers (grain boundaries) and hydrogen trapping sites. LAGBs, with lower interfacial energy compared to HAGBs, exhibit reduced hydrogen adsorption tendency, thereby suppressing crack initiation.
3. Microstructural impacts arise from M-A constituents and cementite phases. Both act as hydrogen aggregation sites that promote microcrack nucleation and propagation, deteriorating HE resistance.
4. Strain rate critically influences HE susceptibility by altering fracture mechanisms. At slower strain rates (e.g., 2×10^{-5} s^{-1}), prolonged hydrogen-dislocation interaction time enables hydrogen permeation from surface to interior regions, exacerbating HE sensitivity through internal crack formation.

Author Contributions: Conceptualization, W.Z. and H.W.; Methodology, W.Z. and L.Z.; Formal analysis, L.Z., G.Z. and P.Z.; Investigation, W.Z., L.Z., X.S. and G.Z.; Data curation, L.Z., X.S. and P.Z.; Writing—original draft, W.Z. and L.Z.; Writing—review & editing, W.Z., L.Z., X.S., G.Z., P.Z. and H.W.; Visualization, L.Z. and P.Z.; Supervision, H.W.; Project administration, H.W.; Funding acquisition, H.W. All authors have read and agreed to the published version of the manuscript.

Funding: This research received no external funding.

Data Availability Statement: The original contributions presented in this study are included in the article. Further inquiries can be directed to the corresponding author.

Conflicts of Interest: The authors declare no conflict of interest.

References

1. Martínez de León, C.; Molina, P.; Ríos, C.; Brey, J.J. Green hydrogen production's impact on sustainable development goals. *Int. J. Hydrogen Energy* **2025**, *142*, 642–653. [CrossRef]
2. Wang, J.; Shuai, Y.; Feng, C.; Zhang, P.; Wang, T.; Lin, N.; Liu, Z. Multi-dimensional mechanical response of multiple longitudinally aligned dents on pipelines and its effect on pipe integrity. *Thin-Walled Struct.* **2021**, *166*, 108020. [CrossRef]
3. Zhang, H.; Zhao, J.; Li, J.; Yu, B.; Wang, J.; Lyu, R.; Xi, Q. Research progress on corrosion and hydrogen embrittlement in hydrogen–natural gas pipeline transportation. *Nat. Gas Ind. B* **2023**, *10*, 570–582. [CrossRef]
4. Abe, J.O.; Popoola, A.P.I.; Ajenifuja, E.; Popoola, O.M. Hydrogen energy, economy and storage: Review and recommendation. *Int. J. Hydrogen Energy* **2019**, *44*, 15072–15086. [CrossRef]
5. Faye, O.; Szpunar, J.; Eduok, U. A critical review on the current technologies for the generation, storage, and transportation of hydrogen. *Int. J. Hydrogen Energy* **2022**, *47*, 13771–13802. [CrossRef]
6. Nazir, H.; Muthuswamy, N.; Louis, C.; Jose, S.; Prakash, J.; Buan, M.E.M.; Flox, C.; Chavan, S.; Shi, X.; Kauranen, P.; et al. Is the H2 economy realizable in the foreseeable future? Part III: H2 usage technologies, applications, and challenges and opportunities. *Int. J. Hydrogen Energy* **2020**, *45*, 28217–28239. [CrossRef]
7. Wang, H.; Cao, S.; Ming, H.; Wan, H.; Hu, Q.; Wang, J.; Han, E.-H. Insight into the hydrogen permeation and hydrogen embrittlement mechanisms of X52 pipeline steel exposed to gaseous hydrogen. *Int. J. Hydrogen Energy* **2025**, *133*, 502–519. [CrossRef]
8. Zhang, R.; Wang, C.; Liu, C.; Zhang, H.; Zhu, M.; Song, Y.; Zhang, T.; Li, Y. Gaseous hydrogen permeation of pipeline steels: A focused review. *Renew. Sustain. Energy Rev.* **2025**, *211*, 115304. [CrossRef]
9. Fan, X.; Cheng, Y.F. Hydrogen pipelines and embrittlement in gaseous environments: An up-to-date review. *Appl. Energy* **2025**, *387*, 125636. [CrossRef]
10. Boukortt, H.; Amara, M.; Hadj Meliani, M.; Bouledroua, O.; Muthanna, B.G.N.; Suleiman, R.K.; Sorour, A.A.; Pluvinage, G. Hydrogen embrittlement effect on the structural integrity of API 5L X52 steel pipeline. *Int. J. Hydrogen Energy* **2018**, *43*, 19615–19624. [CrossRef]
11. Jubica; Claeys, L.; Laureys, A.; De Waele, W.; Schweicher, J.; Depover, T.; Verbeken, K. Gaseous inhibitors: A comprehensive overview on mitigating hydrogen embrittlement in pipeline steels. *Int. J. Hydrogen Energy* **2025**, *136*, 630–642. [CrossRef]

12. Sridharan, V.S.; Verma, V.K.; Narayan, R.L.; Lu, X.; Siwei, D.; Chaudhary, V.; Hua, L.; ZhiLi, D. Hydrogen embrittlement of additively manufactured metallic materials. *Int. J. Hydrogen Energy* **2025**, *121*, 245–272. [CrossRef]
13. Yadav, S.; Jack, T.A.; Zadeh Davani, R.K.; Ohaeri, E.; Szpunar, J. Effect of post-processing heat treatment on hydrogen embrittlement susceptibility of API 5L X70 pipeline steel. *Int. J. Press. Vessel. Pip.* **2022**, *199*, 104762. [CrossRef]
14. Ghosh, G.; Rostron, P.; Garg, R.; Panday, A. Hydrogen induced cracking of pipeline and pressure vessel steels: A review. *Eng. Fract. Mech.* **2018**, *199*, 609–618. [CrossRef]
15. Yan, Y.; Li, L.; Wang, H.; He, N.; Sun, Y.; Xu, L.; Li, L.; Li, H.; Wang, Z.; Zhang, C.; et al. Investigation of hydrogen embrittlement sensitivity of X65 pipeline steel with different compositions employing thermal simulation. *Int. J. Hydrogen Energy* **2024**, *84*, 118–131. [CrossRef]
16. Hou, Y.; Huang, Y.; Li, G. Mechanisms of core-shell construction, interface optimization, and energy level reconstruction for hydrogen embrittlement resistance of yttrium modified X80 pipeline steel. *Int. J. Hydrogen Energy* **2025**, *156*, 150364. [CrossRef]
17. Kim, H.S.; Chang, C.-H.; Lee, H.-G. Evolution of inclusions and resultant microstructural change with Mg addition in Mn/Si/Ti deoxidized steels. *Scr. Mater.* **2005**, *53*, 1253–1258. [CrossRef]
18. Lang, F.; Huang, F.; Yue, J.; Li, L.; Xu, J.; Liu, J. Hydrogen trapping and hydrogen embrittlement (HE) susceptibility of X70 grade high-strength, acid-resistant, submarine pipeline steel with Mg treatment. *J. Mater. Res. Technol.* **2023**, *24*, 623–638. [CrossRef]
19. Liu, D.; Zheng, W.; Hu, S.; Yan, Z.; Hu, R.; Li, G.; Huang, F.; Liu, J. Improvement of deep hydrogen traps induced by modified inclusions and optimized microstructure in pipeline steel with cerium treatment. *Int. J. Hydrogen Energy* **2025**, *111*, 524–535. [CrossRef]
20. Liu, H.; Li, X.; Yang, C.; Luan, Y.; Li, D. Effect of rare earth La on hydrogen diffusion and hydrogen embrittlement susceptibility of 42CrMo martensitic steel. *J. Mater. Res. Technol.* **2025**, *35*, 4805–4818. [CrossRef]
21. Wang, Y.; Xu, X.; Ning, Y.; Chen, Y.; Wang, C.; Liu, C.; Li, Y. Effect of non-metallic inclusions on hydrogen-induced cracking in pipeline steels: A focused review. *Eng. Fail. Anal.* **2025**, *180*, 109875. [CrossRef]
22. Zhang, T.-s.; Wang, D.-y.; Liu, C.-w.; Jiang, M.-f.; LÜ, M.; Wang, B.; Zhang, S.-x. Modification of Inclusions in Liquid Iron by Mg Treatment. *J. Iron Steel Res. Int.* **2014**, *21*, 99–103. [CrossRef]
23. Ran, L.; Chen, S.; Li, B.; Zhang, Z.; Zhang, K.; Wang, B.; Liu, Q.; Jia, S. Improvement of hydrogen embrittlement resistance of X52 pipeline steel by Nb–V composite microalloying design: Hydrogen trap regulation and mechanism. *Int. J. Hydrogen Energy* **2025**, *192*, 152343. [CrossRef]
24. Zha, Y.; Hou, W.; Zhou, M.; Ma, Y.; Gao, K.; Shi, R.; Pang, X. Investigation of the through-thickness hydrogen embrittlement inhomogeneity in X65 seamless pipeline steel. *Int. J. Hydrogen Energy* **2025**, *127*, 871–881. [CrossRef]
25. Lv, L.; Zhuo, J.; Du, Y.; Chen, K.; Dang, G.; Xu, H.; Gao, H.; Guo, Y.; Zheng, S. The effects of hydrogen and microstructure on crack initiation and propagation of X65 pipeline steel. *Corros. Sci.* **2025**, *249*, 112867. [CrossRef]
26. Jack, T.A.; Webb, M.A.; Rahman, K.M.M.; Fazeli, F.; Szpunar, J. Hydrogen uptake and embrittlement behavior in pipeline steels: Insights from slow strain rate testing and synchrotron micro-CT imaging. *Eng. Fail. Anal.* **2025**, *172*, 109419. [CrossRef]
27. Shishvan, S.S.; Csányi, G.; Deshpande, V.S. Strain rate sensitivity of the hydrogen embrittlement of ferritic steels. *Acta Mater.* **2023**, *257*, 119173. [CrossRef]
28. Peng, S.; Zhang, Y.-H.; Chai, C.; Pei, Y.; Zhou, D.; Tian, C. Characterization of quasi-cleavage fracture of pre-strained X80 pipeline steel subjected to SSRT tests in gas hydrogen. *Int. J. Press. Vessel. Pip.* **2025**, *214*, 105448. [CrossRef]
29. Wu, W.; Xia, C.; Fang, Z.; Zhang, X.; Wang, X.; Gong, J.; Li, J. Hydrogen microprinting revealing role of strain-induced defects on hydrogen distribution near austenite crack tip. *Corros. Sci.* **2025**, *257*, 113314. [CrossRef]
30. Thomas, A.; Szpunar, J.A. Hydrogen diffusion and trapping in X70 pipeline steel. *Int. J. Hydrogen Energy* **2020**, *45*, 2390–2404. [CrossRef]
31. Chen, W.J.; Wei, Z.Y.; Zhang, S.H.; Ge, M.K.; Dai, X.; Wu, S. Microstructure evolution and hydrogen embrittlement mechanism of a 2200 MPa press-hardened steel with tempering treatment. *Mater. Charact.* **2025**, *223*, 114955. [CrossRef]
32. Nabizada, A.; Moallemi, M.; Javaheri, V.; Nunes, R.; Verbeken, K.; Depover, T. Hydrogen embrittlement evaluation of wire arc additive manufactured 316L stainless steel: Evidence of hydrogen induced hardening, enhanced decohesion, and assisted localized deformation. *Addit. Manuf.* **2026**, *124*, 105237. [CrossRef]
33. Liu, C.; Li, W.; Gao, X.; Qiao, Y.; Feng, G.; Gao, S.; Li, T.; Chen, X. Tempering-driven evolution of cementite and its influence on hydrogen embrittlement sensitivity. *Int. J. Hydrogen Energy* **2026**, *224*, 154298. [CrossRef]
34. Campari, A.; Ustolin, F.; Alvaro, A.; Paltrinieri, N. A review on hydrogen embrittlement and risk-based inspection of hydrogen technologies. *Int. J. Hydrogen Energy* **2023**, *48*, 35316–35346. [CrossRef]
35. Zhang, S.; Qi, L.; Liu, S.; Peng, Z.; Cheng, Y.F.; Huang, F.; Liu, J. Synergistic effects of Nb and Mo on hydrogen-induced cracking of pipeline steels: A combined experimental and numerical study. *J. Mater. Sci. Technol.* **2023**, *158*, 156–170. [CrossRef]
36. Elsheikh, A.; Ali, A.; Essa, F.A.; Omer, M.A.E.; Abou-Ali, M.G.; Ma, N. Hydrogen embrittlement in storage tank materials and welded joints. *Mater. Today Sustain.* **2026**, *33*, 101282. [CrossRef]

37. Sharma, L.; Chhibber, R. Mechanical properties and hydrogen induced cracking behaviour of API X70 SAW weldments. *Int. J. Press. Vessel. Pip.* **2018**, *165*, 193–207. [CrossRef]
38. Zhang, P.; Laleh, M.; Hughes, A.E.; Marceau, R.K.W.; Hilditch, T.; Tan, M.Y. Effect of microstructure on hydrogen embrittlement and hydrogen-induced cracking behaviour of a high-strength pipeline steel weldment. *Corros. Sci.* **2024**, *227*, 111764. [CrossRef]
39. Zhang, T.; Zhao, W.; Deng, Q.; Jiang, W.; Wang, Y.; Wang, Y.; Jiang, W. Effect of microstructure inhomogeneity on hydrogen embrittlement susceptibility of X80 welding HAZ under pressurized gaseous hydrogen. *Int. J. Hydrogen Energy* **2017**, *42*, 25102–25113. [CrossRef]
40. Momotani, Y.; Shibata, A.; Terada, D.; Tsuji, N. Effect of strain rate on hydrogen embrittlement in low-carbon martensitic steel. *Int. J. Hydrogen Energy* **2017**, *42*, 3371–3379. [CrossRef]

Disclaimer/Publisher's Note: The statements, opinions and data contained in all publications are solely those of the individual author(s) and contributor(s) and not of MDPI and/or the editor(s). MDPI and/or the editor(s) disclaim responsibility for any injury to people or property resulting from any ideas, methods, instructions or products referred to in the content.